



HAL
open science

Emission of gas and Al₂O₃ smoke in gas-Al particle deflagration: experiments and emission modeling for explosive fireballs

Isabelle Ranc-Darbord, Gerard Baudin, Marc Genetier, David Ramel, Pierre Vasseur, Julien Legrand, Vincent Pina

► To cite this version:

Isabelle Ranc-Darbord, Gerard Baudin, Marc Genetier, David Ramel, Pierre Vasseur, et al.. Emission of gas and Al₂O₃ smoke in gas-Al particle deflagration: experiments and emission modeling for explosive fireballs. International Journal of Thermophysics, 2018, 39 (3), pp.36. <10.1007/s10765-018-2360-9>. <hal-02304920>

HAL Id: hal-02304920

<https://hal.parisnanterre.fr/hal-02304920v1>

Submitted on 3 Oct 2019

HAL is a multi-disciplinary open access archive for the deposit and dissemination of scientific research documents, whether they are published or not. The documents may come from teaching and research institutions in France or abroad, or from public or private research centers.

L'archive ouverte pluridisciplinaire **HAL**, est destinée au dépôt et à la diffusion de documents scientifiques de niveau recherche, publiés ou non, émanant des établissements d'enseignement et de recherche français ou étrangers, des laboratoires publics ou privés.



HAL Authorization

Emission of gas and Al₂O₃ smoke in gas-Al particle deflagration: experiments and emission modeling for explosive fireballs

Isabelle Ranc-Darbord^{1,a)}, Gérard Baudin², Marc Genetier², David Ramel^{1,b)}, Pierre Vasseur^{1,c)}, Julien Legrand², Vincent Pina¹

¹Laboratoire Energétique Mécanique Electromagnétisme, UPL, Univ Paris Nanterre

50 rue de Sèvres, 92410, VILLE d'AVRAY, FRANCE– 33(0)1 40 97 48 71

²CEA, DAM, GRAMAT, F-46500, GRAMAT, FRANCE

Emission of gas and Al₂O₃ smoke within the deflagration of H₂-O₂-{N₂-CO₂}-Al particles has been studied in a closed combustion chamber at pressures of up to 18 bar and at gas temperatures of up to 3700 K. Measurements of radiance intensity were carried out using a 5 wavelength pyrometer (0.660, 0.850, 1.083, 1.260, 1.481 μm) and a grating spectrometer in the range (4.10-4.30) μm. In order to characterize the aluminum-oxide smoke size and temperature, an inversion method has been developed based on the radiation transfer equation and using pyrometer measurements and thermochemical calculations of Al₂O₃ smoke volume fractions. Temperatures in combustion gas have been determined using a method based on the assumed blackbody head of the 4.26 μm CO₂ emission line and on its spectral shift with pressure and temperature. For validation purpose, this method has been applied to measurements obtained when calibrated alumina particles are injected in a combustion chamber prior to gaseous deflagrations. This mathematical inversion method was developed to investigate explosive fireballs.

Symbols

d_p	particle diameter (μm)
f_v	volume fraction
K_λ	spectral absorption coefficient (m ⁻¹)
k	absorptive part of the complex refractive index
L_λ	spectral radiance (W.m ⁻² .sr ⁻¹ .μm ⁻¹)
L_λ^0	spectral blackbody radiance
m	complex refractive index
n	refractive part of the complex refractive index
P	pressure (bar)
T	temperature (K)
x	molar fraction or abscissa

^{a)}corresponding author: isabelle.ranc@parisnanterre.fr

^{b)}current address: FEMTO-ST, Université de Belfort – Montbéliard, 2 avenue Jean Moulin, 90000 BELFORT, FRANCE

Greek letters

ε_λ	emissivity
β_λ	extinction coefficient
σ_λ	scattering coefficient or standard deviation
λ	wavelength (μm)

I. INTRODUCTION

Detonation of solid high explosives (HE) is a supersonic reactive shockwave propagating at high velocities (6 km/s to 9 km/s) which converts the solid explosives into detonation products (DP) composed of gases and particles (aluminum, carbon, etc.) at high pressures, 20 GPa to 40 GPa, and high temperatures (3000 K to 5000 K). Chemical reactions behind the detonation front are very fast (a few nanoseconds). Its chemical energy is released in a thin reaction zone (less than 1 mm for many HE) leading to a high-temperature high-pressure peak. This peak is then followed by a release wave along which pressure and temperature drop down. The interaction between the detonation wave with the surrounding air generates both a shockwave and a release wave which propagates respectively in air and in DP. At the early stage of the DP expansion in air, the shock-heated air is warmed enough so as to be ionized. Many authors consider the fireball to be the DP – air interface [1-2]. Due to the strong radiations of the ionized air, this fireball cannot be observed in the visible range, even by fast-speed color cameras, at the beginning of DP expansion in air. As the shock wave propagates in air far from the explosive charge, its pressure and temperature decrease. Then, the fireball becomes visible on fast-speed videos when air ionization stops. A selection of photographs, extracted from a fast-speed video recording of a fireball created by the detonation of a 0.385 kg spherical HMX pressed charge, is presented on Fig. 1. It illustrates the fireball expansion and the air-shock propagation at a rate of 30 000 fps. At the early stage of expansion (66 μs), the photon emission of ionized air saturates the camera so that the fireball is not visible. Concentrations of the main species in the fireball determined through real gas thermochemical equilibrium computations (CHEETAH code / BKW-C equation of state) are 3.7 mol/kg of explosive for N_2 , 2.1 mol/kg for H_2O , 1.4 mol/kg for CO_2 , 2.8 mol/kg for CO and 1.6 mol/kg for H_2 . Solid carbon appears at large fireball expansions. The fireball velocity is around 8 km/s at the beginning of the expansion and drops down to 2 km/s.

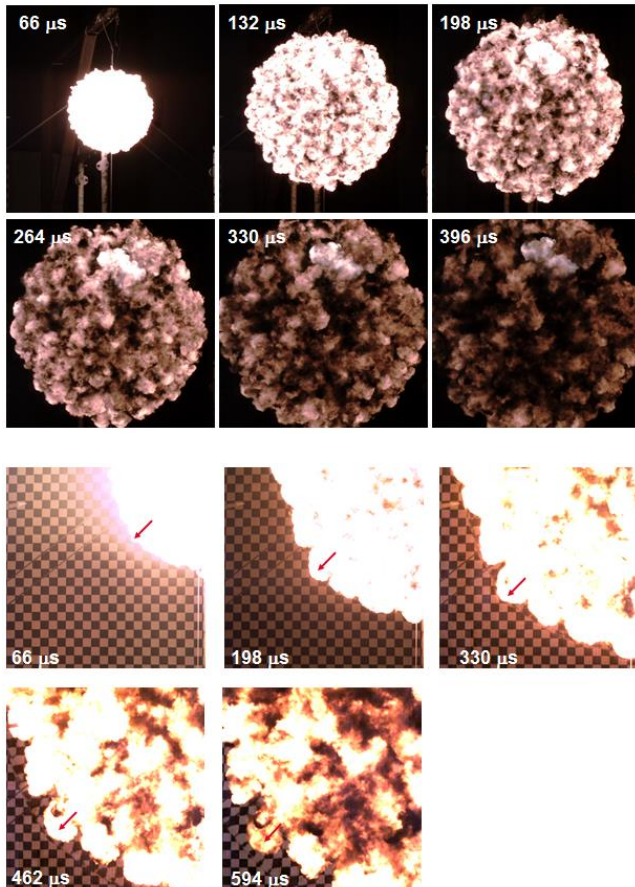


FIG. 1: Evolution of the fireball of a 0.385 kg spherical charge of pressed HMX charge ($\rho_0 \sim 1860 \text{ kg/m}^3$), high-speed video at 30 000 fps, at exposure time $1/253000 \text{ s}$ and $1/266000 \text{ s}$ (zoom) on the same experiment, performed at CEA Gramat. The background grid is 5 cm.

In the case of an explosion in a closed vessel, secondary shock waves reflect on the walls of the vessel at high velocities, leading to a homogeneous pressure after several reflections, contrary to the temperature field which keeps in memory the temperature field in the vessel for the time period of the first few milliseconds. It is also known that a secondary turbulent combustion occurs between air and the DP due to the presence of particles (carbon and aluminum), H_2 , CO and hydrocarbon components within the DP. High-speed videos of the explosion of a melt-cast TNT spherical charge inside a small scale bunker suggest the inhomogeneity of temperature [2]. Due to limited knowledge of this secondary combustion, its modeling has been difficult. Hence, experimental data are necessary to discriminate different models in literature. Generally, measurements focus on overpressures in air and luminance temperatures.

To obtain real temperatures or to simulate fireball radiation, thermal radiation properties are necessary: the spectral absorption-scattering coefficients in the pressure and temperature ranges achieved during DP expansion. Chapman-Jouguet isentropic curve calculations [3] obtained with the CHEETAH code suggests that DP have temperatures in the range of 700 K to 4000 K whereas pressures are in the range of 5 bar to 400 bar a few

milliseconds after detonation. In these conditions, typical aluminum concentrations before combustion are less than 400 g/m³.

The dominant gases in the DP are listed in Table 1 together with their main absorption lines, given by currently used databases, Hitran [4-5], Hitemp [6] and CDS [7]. These databases were developed for temperatures up to 5000 K for CO₂ in Hitemp and CDS, but at ambient pressure only. The dominant DP species emitting in the spectral range of interest (visible-IR) associated to fireball thermal effects are H₂O, CO₂, CO, solid carbon, aluminum and alumina. The problem then becomes more complex when aluminum is present in HE.

TABLE 1: Band location (wavelength) of the main absorption lines [8]

Species	up to 5 μm
N ₂	4.30 μm
CO	4.70 μm 2.35 μm
CO ₂	4.26 μm 2.70 μm 2.00 μm
H ₂ O	2.70 μm 1.87 μm 1.38 μm 0.96 μm 0.82 μm 0.72 μm 0.65 μm 0.59 μm
AlO	0.464 μm 0.486 μm 0.507 μm (three main)
Al particles	Continuous spectrum
Al ₂ O ₃ particles	Continuous spectrum
Solid C particles	Continuous spectrum

The objectives of this work are (i) to understand how aluminum combustion and aluminum oxide smoke contribute to the radiation in the pressure range of 1 bar to 18 bar and at gas temperatures of up to 3700 K, (ii) to measure pressure-temperature state of DP in these ranges in order to validate thermochemical computations. By limiting the study to the visible-near infrared 520 nm to 1480 nm range (VIS-nIR) and to the infrared 4.1 μm to 4.3 μm range (IR), the dominant radiation effects are those of CO₂ and Al₂O₃ smoke. In this study, CO₂ and Al₂O₃ particles are heated by a controlled H₂-O₂-diluent deflagration propagating inside a cylindrical closed combustion chamber at pressures up to 18 bar and gas temperatures of up to 3700 K. The diluents are N₂ and CO₂.

II. REVIEW ON WORKS DEDICATED TO AL₂O₃ SMOKE IN GAS-AL DEFLAGRATION

Many studies on aluminum particle combustion characteristics have been published [9-11]. Nevertheless, all of them dealt with lower pressures than the pressure range of this work. Badiola et al [9] studied the combustion characteristics of 1 μm to 22 μm aluminum particles in O₂/N₂ mixtures using pyrometry. Zhu et al. [10] studied aluminum powder in CO₂/O₂ mixtures through thermogravimetric analyses and X-Ray diffraction measurements. Using a resolved spectroscopy technique, Goroshin et al [11] thoroughly studied the spectra emitted by stabilized Bunsen-type flames of 5 μm aluminum suspensions in air and oxygen-argon/helium mixtures. The spectral

measurements have been performed in the nUV-Vis-nIR range 350 nm to 1000 nm at an Al concentration of 500 g/m³. The spectra clearly exhibit a continuous spectrum and the blue-green B²Σ⁺ - X²Σ⁺ AlO vapor lines. In [12], the gas temperature was derived from these lines. A polychromatic fitting of the low resolution spectra continuum to Planck's law was used to compute the particle cloud temperature. The light emission cross-section model is based on the Rayleigh diffusion limit considering a 1/λ decrease of the absorption index of the molten bulk aluminum oxide. The temperature distribution lies between 3000 K and 3550 K across the flame. These data are useful for understanding the basics of dust cloud combustion. However, the emission model proposed in Goroshin's paper is not deduced rigorously from the theory of particle scattering. A more rigorous determination of the emission model can be achieved from the work of Parry and Brewster [13] by using an inverse solution of optical properties of the continuous spectra. These studies were performed at ambient pressure. They cannot be directly applied to the DP or to the deflagration waves in which pressures of about 10 bar to 30 bar can be observed.

In another work, Goroshin et al [14] used a pyrometer and several spectrometry techniques at the same wavelength range to study the emission of fireballs from metalized explosives. Several explosives were investigated, Al-Nitromethane mixtures among them. The spectra of the latter are similar to those of an Al suspension in air or O₂. No temperatures were deduced from these spectra, but the reliability of such techniques is clearly demonstrated.

Useful data were also obtained by Cashdollar and Zlochover [15] who studied the explosion hazard conditions of metals and other elemental dust clouds (2 μm to 180 μm size) in air using a 20 L test chamber. The authors used a six wavelength IR pyrometer in the range 1.57 μm to 5.00 μm to measure the dust cloud temperature. Explosion pressure, rate of pressure rise and explosion temperature, were determined as a function of the dust concentration for pressures and temperatures respectively below 10 bar and 2800 K. The experimented dilution of Al was 330 g/m³ of Al. These authors used a grey body emissivity model to compute the dust cloud temperatures from radiation measurements. In the IR 2.00-4.26 μm wavelength range, CO₂ has 3 dominant radiation lines, revealing a discontinuous emission spectrum.

III.THE COMBUSTION CHAMBER

The combustion chamber, designed in a previous study [16], is a closed stainless steel tube of 600 mm length and of 150 mm internal diameter (Fig. 2). The tube is closed by two stainless steel flanges. The front one is equipped with a spark igniter (A). The optical access is a sapphire window (20 mm diameter, 5 mm thickness) placed on the cylinder axis through the end flange (B). The injection of the different gases (C) within the vacuum chamber is controlled by partial pressure measurements using a transmitter Kristal RAG25A2BC1H with an accuracy of 1 mbar.

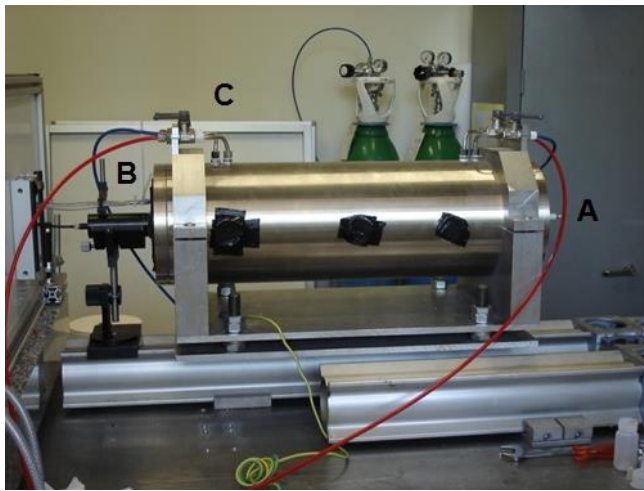


FIG. 2: Combustion chamber.

The particle injection system is a horizontal fluidized bed placed inside the gas injection tube. The system has been designed to maximize the suspension time. The quality of the particle cloud has been examined by a laser sheet video-tomography. The laser sheet, obtained on a limited sector of 23° , is created inside the combustion chamber through the lateral sapphire windows placed at different distances from the spark igniter. Two laser sheet tomography examples, illustrating the difference between sedimentation and no-sedimentation of the particle clouds, are presented on the right side of Fig. 3.

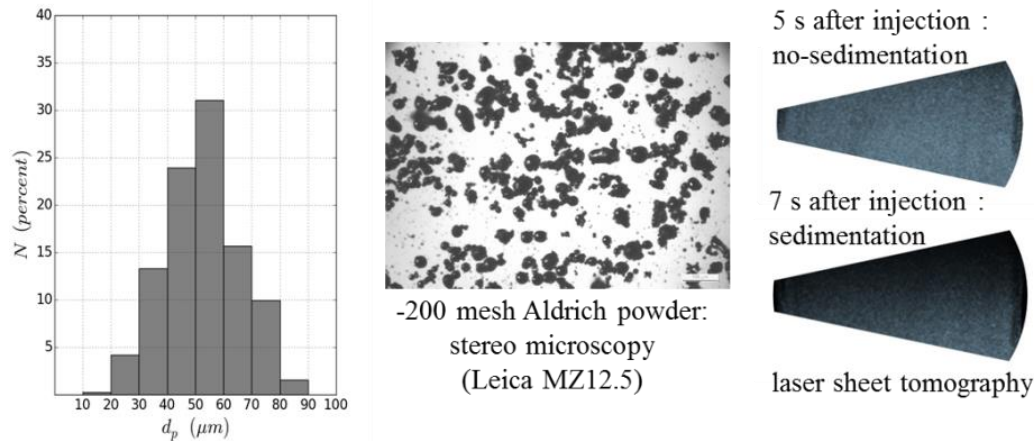


FIG. 3: -200 mesh Aldrich powder stereo microscopy, particle size distribution and examples of laser tomography.

N_2 , air, CO_2 and H_2 are successively injected in the chamber. The adopted fluidization technique consists in introducing particles within the last gas flow inside the chamber in order to induce a strong turbulence. This turbulence enables to maintain the particle cloud in suspension during around 6 s, thus ensuring a good gas-particle mixing. The delay time to fire must be reduced as possible (less than 7 s) in order to minimize deposition on the chamber wall. A cloud of suspended particles is needed in order to properly account for their volume fraction in the thermophysical model of the cloud radiation. This particle injection system enables controlling the particle volume fraction inside the chamber by quantifying the mass introduced into the fluidized bed.

Two types of particles are injected: aluminum and alumina. The aluminum-powder is the -200 mesh Aldrich powder with the product specification $<75 \mu\text{m}$ and $\geq 99.95\%$ purity. The particle size distribution is plotted on the left side of Fig. 3. The Sauter diameter d_{32} of the particles is about 59 μm . Its density is 2700 kg/m^3 at 298 K. Aluminum is highly reactive in $\text{H}_2\text{-O}_2\text{-CO}_2$ gaseous mixtures and generates an Al_2O_3 smoke at the end of combustion. The mass of aluminum powder introduced in the chamber is 4 g, determined so as to obtain a volume fraction of 1.4×10^{-4} and a dilution of 400 g/m^3 . The aluminum oxide powder is a -325 mesh alpha- Al_2O_3 CERAC with a purity superior to 99.99%. Particle sifters are used to obtain calibrated particles of around 44 μm size. The particle density is 3900 kg/m^3 at 298 K. Its melting temperature is 2323 K at 1 atm. As its evolution in the range 1 bar to 20 bar is small enough, it has been considered constant in the following. The mass control system leads to a volume fraction of 0.967×10^{-4} . As the added alumina introduced in the gas phase behaves like an inert material [17], the experiments done with this powder will be shown to validate the inversion method developed for the Al_2O_3 smoke cloud (section VII-B). The mean particle size d_p and the volume fraction f_v of the alumina suspension

have been selected so as to be in the independent scattering regime in the $\frac{\pi d_p}{\lambda} - f_v$ plane [8,18]. This will be also the case for the Al_2O_3 smoke generated by the aluminum particle combustion.

The dynamic pressure induced by the $\text{H}_2\text{-O}_2$ -diluent deflagration is measured by a piezoelectric sensor Kistler Model 6061b, placed above the sapphire window at the end flange (B). The radiation intensity emitted by the mixture of gases and particles is collected through the sapphire window by a fast CCD camera coupled to a grating spectrometer (Fig. 4) or by a six wavelengths optical pyrometer (Fig. 5). The whole bench (CCD camera, spectrometer, and optical collecting system) is placed under a controlled N_2 atmosphere to limit ambient H_2O and CO_2 absorptions. The optical measuring devices are described in the following section.

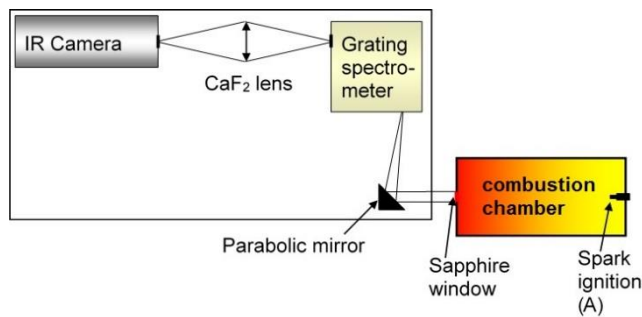


FIG.4: Experimental setup for IR spectral measurements

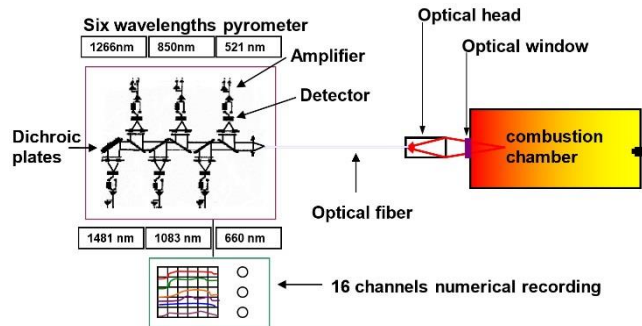


FIG.5: Experimental setup for Visible-IR spectral measurements

IV. THE OPTICAL MEASURING DEVICES

The IR measuring device (Fig.4) is composed of a parabolic mirror, a JOBIN YVON TRIAX 180 grating spectrometer, a CaF_2 lens and a fast CCD camera ORION of CEDIP IR system (now marketed by FLIR). The grating is blazed at 2500 nm with a groove density of 120 graduations per millimeter. The flux is collected as a parallel light beam from the sapphire window. The radiation entering the spectrometer is focused by the parabolic mirror. At the spectrometer outlet, the image of the spectrum is collected through a CaF_2 lens on the IR camera matrix. The spectral range of the camera is $1.5 \mu\text{m}$ to $5.0 \mu\text{m}$ and the frame rate is 6000 Hz. The analysis of the signal is limited to the range of $4.1 \mu\text{m}$ to $4.3 \mu\text{m}$, within which the optical system is achromatic.

For pyrometer measurements, the previous device is replaced by an optical probe to collect the radiation flux in the VIS-nIR range, connected to the pyrometer by an optical fiber. The pyrometer splits the flux on 6 wavelengths: 0.521, 0.660, 0.850, 1.083, 1.260 and 1.481 μm . The detectors are Si photodiodes for the first three wavelengths and InGaAs for the last three. The electric signals are amplified and recorded using numerical scopes. No significant signals have been obtained at the 0.521 μm wavelength.

For both measuring devices, the records are synchronized on the spark igniter pulse. The wavelength – pixel correspondence on the IR CCD is calibrated with the spectrum of the CO_2 4.26 μm emission band of a Bunsen burner methane flame placed behind the spark igniter hole. The electric signal – luminance calibration is performed in the range 1000 K to 1773 K on a blackbody PYROX placed at the back of the combustion chamber, instead of the flange A (in Fig.2). The intensity is then obtained in $\text{W}\cdot\text{m}^{-2}\cdot\text{sr}^{-1}\cdot\mu\text{m}^{-1}$.

All radiances which will be illustrated from now have been measured when the flame front quenches at the end of the chamber or equivalently when the measured pressure reaches its maximum [16]. At this time, the radiance of hot deflagration gases is free of any absorption of fresh gases, otherwise still present ahead of the flame front when the deflagration propagation remains unfinished. Numerical simulations performed by Davidenko [19] exhibit a uniform pressure inside the combustion cylinder at each step of the flame propagation: in such a closed configuration, no gas cooling occurs behind the flame during its propagation. When the deflagration reaches the sapphire window, pressure, temperature and gas concentrations are uniform and correspond to an adiabatic constant volume explosion (no heat exchange between the gases and the vessel walls for the flame velocities obtained here). This has also been demonstrated by Santhanam and Dreizin [20] when using perfect gas equations of state with a constant polytropic index for both unreacted gases and deflagration products. Thus, the spectra obtained at the end of deflagration propagation can be easily analyzed by considering a uniform column of gas – particles.

V. METHODS DEVELOPED TO DETERMINE GAS TEMPERATURE AND PARTICLE CLOUD EMISSIVITY AND TEMPERATURE

Gas temperature on the one side, alumina particle cloud temperature and mean diameter on the other side, can be determined from measured radiances, by assuming a known volume fraction and an adequate absorption-scattering Al_2O_3 droplet model to integrate the radiative transfer equation. Particle mean size and temperature are calculated from VIS-nIR measurements. Gas temperature is determined from the IR radiances.

A. Determination of gas temperature

At the emission band located at 4.26 μm , broadening of the CO_2 lines due to pressure and temperature increase is exploited. Computations of the CO_2 spectra in the limited range of 4.13 to 4.20 μm at several pressure-temperature couples, using the HITRAN 2012 database, illustrate this behavior in Fig.6. Beyond 4.17 μm , heated CO_2 is opaque in the experiments whereas CO_2 is transparent at ambient temperature, so atmospheric CO_2 does not contribute to the signal). The originality of the method proposed here is the exploitation of this property to determine the temperature of the deflagrating gases using a spectroscopic technique and Planck's law [21],

$$L_{\lambda}^0(T) = \frac{c_1 \lambda^{-5}}{\exp\left(\frac{c_2}{\lambda T}\right) - 1} \quad (1)$$

$$c_1 = 2c^2 h = 1.19 \times 10^8 \text{ W.m}^{-2}.\mu\text{m}^4.\text{sr}^{-1} \text{ (} c: \text{ speed of light in vacuum, } h: \text{ Planck's constant)}$$

$$c_2 = \frac{hc}{k_B} = 14388 \text{ } \mu\text{m.K (} k_B \text{ is Boltzmann's constant).}$$

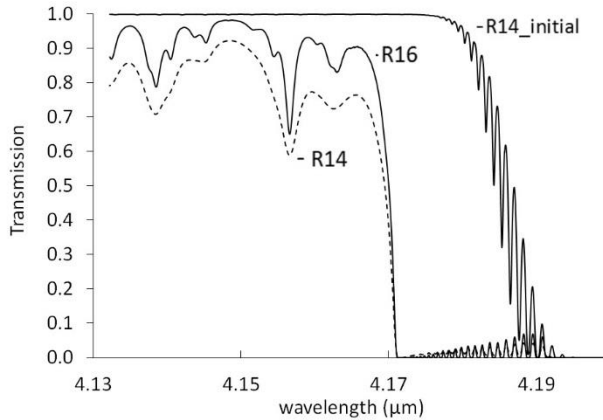


FIG.6: Transmission of a 600 mm depth gas column under several thermodynamic conditions and at several dilutions: Shots R14 and R16 at the final deflagration state with CO_2 molar fractions of 0.057 (R14) and 0.1622 (R16), and Shot R14 at ambient state. The pressure and temperature conditions are given in Table 2. The calculations were performed using Hitran on the Web 2012 (<http://hitran.iao.ru>).

Typical spectra and pressure evolutions are given in Fig. 7, Fig. 8 and Fig. 9 for two levels of the deflagration pressure. They correspond to $\text{H}_2\text{-O}_2$ stoichiometric combustions in $\text{N}_2\text{-CO}_2$ mixtures with the initial compositions reported in Table 2 (shots R16 and R17). The maximum combustion pressure and IR radiation is achieved when the expanding flame reaches the sapphire window and quenches. Fig. 7 and Fig. 8 clearly exhibit the broadening of the CO_2 emission lines at the band location 4.26 μm due to the increase of pressure and temperature conditions during the flame propagation. The maximum combustion pressures and temperatures will be further compared to equilibrium thermochemical computations obtained with SIAME, a new thermochemical code developed at the CEA for energetic material combustion, deflagration and detonation. 32 experiments were performed in various

initial configurations in the ranges 6-20 bar and 2200-3700 K. Many experiments were performed and analyzed twice to ensure reproducibility (see Table 2). No carbon soot production has been observed as suggested by the cleanliness of the internal surface of the combustion chamber after the experiments. This is also retrieved by the thermochemical computations.

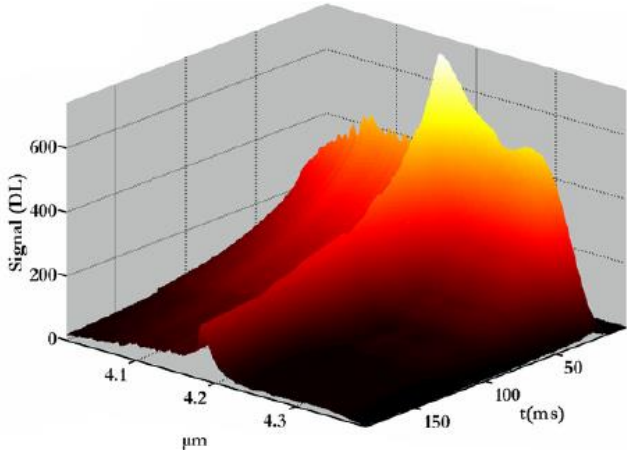


FIG. 7: Typical measured radiance for Shot R16 (P=7.9 bar). See the conditions in Table 2.

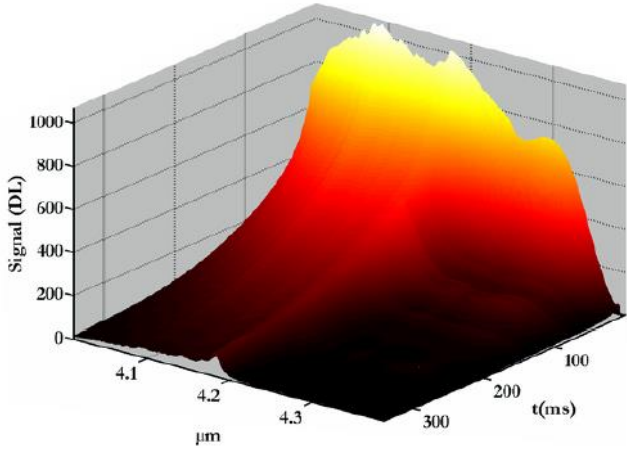


FIG. 8 Typical measured radiance for Shot R14 (P=16.1 bar). See the conditions in Table 2.

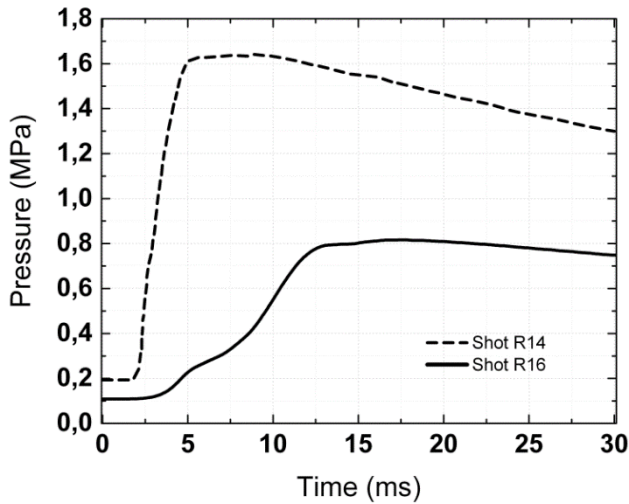


FIG.9: Typical measured pressures for Shots R16 (P=7.9 bar) and R14 (P=16.1 bar)

B. Determination of the Al_2O_3 smoke mean size and temperature

Al_2O_3 smoke is formed by aluminum combustion following a complex chemical scheme. The combustion of aluminum powder with CO_2 and H_2O leads to final products composed of Al_2O_3 . Many papers have addressed the physics of aluminum combustion. Beckstead [22] summarized all the studies until 2002 with around 400 experimental data and proposed the most recent chemical scheme [23] for aluminum – oxygen combustion with eight elementary reactions comprising surface reactions, evaporation/dissociation, gas phase chemistry and condensation. These elementary reactions produce AlO gas having emission lines in the green-blue wavelength range. These lines are well-known and well-modeled at atmospheric pressure. At high pressures (typically > 5 bar in the experiments of this study), no valid modeling is still available. In a deflagration, the aluminum combustion is generally assumed to generate a bimodal Al_2O_3 particle size distribution. Indeed, Al_2O_3 smoke is composed both of large particles due to alumina condensation on the surface of aluminum particles and of submicron ones due to the condensation of the vapor-phase alumina in the gaseous products (Parry and Brewster [13]). The alumina volume fraction is small enough to consider independent scattering [8]. Under this assumption, the bimodal-distributed alumina particles follow both optical geometry diffusion (large particles) and Rayleigh diffusion (micron particles) regimes. Following Parry and Brewster [13], the radiation of submicron particles dominates in a range of possible diameters of $0.86 \mu\text{m}$ to $1.08 \mu\text{m}$ due to their large specific surface area. The diffusion of large particles of Al, covered by Al_2O_3 , can thus be neglected. Generally, authors consider a Rayleigh scattering regime for the micron particles. Parry and Brewster [13] used the Mie scattering theory. As the size range of particles is of the same order as the wavelength range of our optical pyrometer, the Mie scattering theory will further be used.

Complex refractive index value for alumina is assumed by $m = n - ik = 1.7 - i0.05$ independently of the wavelength according to French [24]. Bityukov and Petrov [25] published a critical compilation of available experimental data on the absorption and refractive indexes of alumina between 2320 K and 3000 K. More recently, Lynch et al [26] proposed models for the emissivity of micro and nano-alumina particle clouds heated by a reflected shock wave in shock tube experiments. These models have been established with the use of a visible emission spectrometry technique, but they have neglected the influence of the volume fraction of particles in the cloud. In their configuration, motion of the particles during the shock wave propagation hardens the estimation of their volume fraction. Volume fraction of particles is known to strongly influence the emissivity of a particle cloud which can then be optically thin or thick, following the Mie theory.

The good agreement between the experimental and calculated absorption and refractive indexes obtained by Parry and Brewster [13] leads us to retain their model. It is based on the classical Lorentz dispersion theory of the complex dielectric function $\epsilon = \epsilon' + i\epsilon''$ where:

$$\epsilon' = n^2 - k^2 = 1 + \sum_j^N \text{oscillators} \frac{\eta_{pj}^2 (H_{0j}^2 - \eta^2)}{(H_{0j}^2 - \eta^2)^2 + \gamma_j^2 \eta^2} \quad (2)$$

$$\epsilon'' = 2nk = \sum_j^N \text{oscillators} \frac{\eta_{pj}^2 \gamma_j \eta}{(H_{0j}^2 - \eta^2)^2 + \gamma_j^2 \eta^2} \quad (3)$$

η_{pj} being the plasma wavenumber, H_{0j} the effective wavenumber, η the wavenumber, and γ_j the damping coefficient. In this model, $H_{0j}^2 = \eta_{0j}^2 - \frac{\eta_{pj}^2}{3}$, with the characteristic wavenumber η_{0j} .

For alumina, two oscillators were considered by Parry and Brewster [13] with wavelengths $\lambda_{01} = \frac{1}{\eta_{01}} = 0.1107 \mu\text{m}$ and $\lambda_{02} = \frac{1}{\eta_{02}} = 17.57 \mu\text{m}$. The dispersion parameters η_{pj}^2 and γ_j^2 are represented with polynomial functions such as:

$$a_0 + a_1 T^* + a_2 T^{*2} + a_3 T^{*3} + a_4 T^{*4} \quad (4)$$

depending on a scaled temperature T^* given by:

$$T^* = \frac{T - 2320}{3000 - 2320} \quad (5)$$

The parameters are given in [13]. Temperature and wavelength evolutions of the complex index are compared to experimental values in Fig. 10. This model is strictly valid in the temperature range 2320 K to 3000 K and in the wavelength range of 0.5 μm -5 μm corresponding to the experimental data of Bityukov and Petrov [25]. It can

be extrapolated to temperatures higher than 3000 K with $\gamma_j^2 = \gamma_j^2(T^* = 1)$ and $\eta_{pj}^2 = \eta_{pj}^2(T^* = 1)$ in order to preserve the physical tendencies for the absorptive and the refractive indexes.

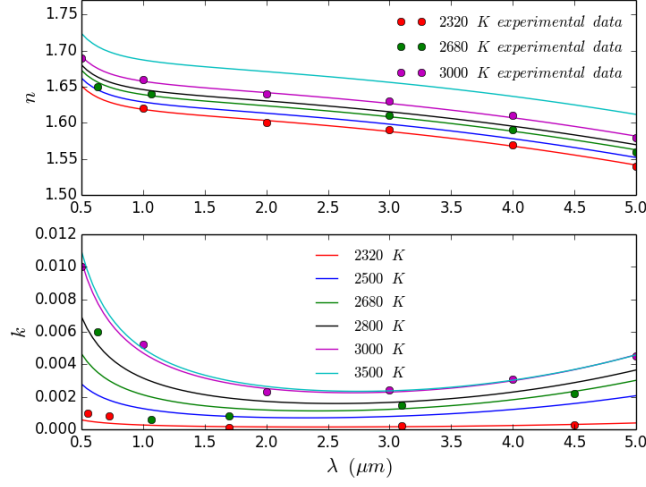


FIG. 10: absorptive and refractive indexes versus the temperature and the wavelength and experimental data.

The absorption and scattering coefficients K_λ and σ_λ are computed using the Python code which can be found on the page <https://code.google.com/p/scatterlib/wiki/Spheres>. The initial version of this code is due to Bohren and Huffman [27].

In the VIS-nIR range, the only emitting gas is H_2O with low intensity ($\sim 10^{-5} \text{ W}\cdot\text{cm}^{-2}\cdot\text{sr}^{-1}\cdot\text{cm}^{-1}$ at the temperatures and pressures considered in this work). The spectrum is clean of other deflagration gas emission lines.

In [13], the equation of radiative transfer for a non-emitting one-dimensional parallel slab is solved by a discrete ordinate method. This method is useful for a problem with a well-characterized refractive index for low-pressure combustion. However $\text{H}_2 - \text{O}_2$ deflagration leads to a pressure range of 8 bar to 20 bar. As no data has been found in the literature for the refractive index evolution in this pressure range, a simpler method based on a two-stream approximation to radiative transfer has thus been assumed to be a sufficient approach. Meador and Weaver [28] proposed unified two-stream equations for plane parallel atmospheres with assumptions of time independence, elastic scattering, no internal sources and no thermal emission, with incident collimated flux. An adaptation of these equations, for an emitting media without incident flux, is proposed for the diffused radiance:

$$\frac{dL_\lambda^+}{d\tau} = -\gamma_1 L_\lambda^+ + \gamma_2 L_\lambda^- + \gamma_3 L_\lambda^0(T) \quad (6)$$

$$\frac{dL_\lambda^-}{d\tau} = \gamma_1 L_\lambda^- - \gamma_2 L_\lambda^+ - \gamma_3 L_\lambda^0(T) \quad (7)$$

where $L_\lambda^0(T)$ is Planck's law, and L_λ^+ the forward radiance, L_λ^- the backward radiance (Fig. 11), $d\tau = \beta_\lambda(\lambda, T(x))dx$, with β_λ being the extinction coefficient ($\beta_\lambda = K_\lambda + \sigma_\lambda$). The coefficients γ_i depend on the two-stream approximation considered. The simplest one is the hemispheric constant approximation in which the γ_i are given by the expressions:

$$\gamma_1 = \frac{1}{2}(1 - g\omega_\lambda) + \frac{1}{2}(1 - \omega_\lambda) \quad (8)$$

$$\gamma_2 = \frac{1}{2}(1 - g\omega_\lambda) - \frac{1}{2}(1 - \omega_\lambda) \quad (9)$$

$$\gamma_3 = (1 - \omega_\lambda) \quad (10)$$

where g is the asymmetric factor and $\omega_\lambda = \frac{\sigma_\lambda}{\beta_\lambda}$ is the particle cloud albedo.

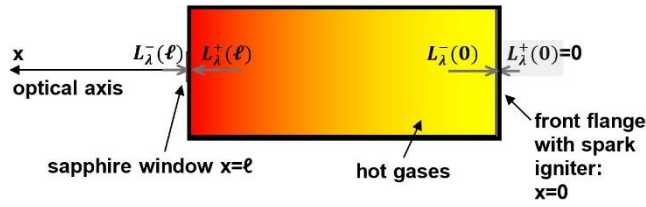


FIG.11: schematic two-stream approximation in the combustion chamber

The boundary conditions considered in the configuration of this study are zero fluxes both through the sapphire window ($L_\lambda^-(\tau_\ell) = 0$, with $\tau_\ell = \beta_\lambda \ell$, ℓ being the deflagration cell length), and from the back flange of the chamber ($L_\lambda^+(\tau = 0) = 0$). Indeed, temperature on the internal surface, evaluated from the heat conduction transfer between gases and steel, is in the range of 300-310 K. The only additional possible source of parasite radiations may come from the spark plug.

As previously stated, the temperature, pressure and particle concentration are uniform at the end of the deflagration propagation. In these conditions, equations (6) and (7) of radiation transfer in a plane, parallel and uniform media, admit an analytical solution for the net flux $L_\lambda(\tau_\ell) = L_\lambda^+(\tau_\ell) - L_\lambda^-(\tau_\ell)$ received on the optical head of the pyrometer:

$$L_\lambda(\tau_\ell) = L_\lambda^0(T) \left(1 - \exp(-\Gamma\tau_\ell) - 2 \frac{r_\infty(r_\infty \exp(-\Gamma\tau_\ell) - 1)}{\exp(\Gamma\tau_\ell) - r_\infty^2 \exp(-\Gamma\tau_\ell)} \sinh(\Gamma\tau_\ell) \right) \quad (11)$$

where $\Gamma = \sqrt{(1 - \omega_\lambda)(1 - \omega_\lambda g)}$ and $r_\infty = \frac{\sqrt{1 - \omega_\lambda g} - \sqrt{1 - \omega_\lambda}}{\sqrt{1 - \omega_\lambda g} + \sqrt{1 - \omega_\lambda}}$

ω_λ , β_λ , and g are computed from the Mie scattering theory. The cloud emissivity is therefore:

$$\varepsilon_\lambda(\ell, d_p, f_v) = \frac{L_\lambda}{L_\lambda^0} = 1 - \exp(-\Gamma\tau_\ell) - 2 \frac{r_\infty(r_\infty \exp(-\Gamma\tau_\ell) - 1)}{\exp(\Gamma\tau_\ell) - r_\infty^2 \exp(-\Gamma\tau_\ell)} \sinh(\Gamma\tau_\ell) \quad (12)$$

Temperature, diameter of the molten alumina droplets and their volume fraction can be deduced from radiance pyrometric measurements with the help of a mathematical inversion of this analytical solution. This inversion method assumes negligible emissions of both H₂O and large particles generated by alumina condensation on the surface of aluminum particles. The mathematical inversion consists in finding a solution for which a given objective function reaches its global minimum. The objective function is here chosen in the following form:

$$J = \frac{1}{2} \sum \lambda \left(\frac{L_{\lambda}^{measured} - L_{\lambda}^{calculated}}{\sigma_{\lambda}^{measured} + \sigma_{\lambda}^{noise}} \right)^2 \quad (13)$$

where $\sigma_{\lambda}^{measured}$ is the standard deviation of the radiance measurements and σ_{λ}^{noise} the standard deviation of the noise at the wavelength λ . These have been quantified at 3 to 6 % of the radiance measurements, depending on the wavelength.

We thoroughly studied the sensitivity of the net flux L_{λ} to the volume fraction f_v , the particle mean diameter d_p and the temperature T_p for values in the respective ranges of 4×10^{-5} - 4×10^{-4} , 1-20 μm and 2320-3000 K. This sensitivity analysis exhibits a complex behavior of the net flux characterized by a high sensitivity to temperature and to the particle diameter. To get rid of Planck's law sensitivity to temperature, the evolution of spectral emissivity ε_{λ} with the previous three parameters is analyzed as illustrated on Fig. 12. The oscillations of the spectral emissivity observed on this figure are physically due to the two-oscillators representation of the dielectric function associated with the Mie scattering theory. The gray body behavior (independence on λ for ε_{λ}) in the visible wavelength range is obtained for large particle sizes only. A full mathematical inversion, for f_v , d_p and T_p , presents several local minima. For alumina particle diameters of about 1 μm , which is the size obtained by Parry and Brewster [13] in a propellant combustion, the sensitivity to the volume fraction is small. Thus, the volume fraction which were considered here is the maximum value obtained by the thermochemical code SIAME when considering a fully aluminum combustion. Special attention was paid to the minima of J obtained with different initial values of d_p and T_p in the optimization process, so that the optimized solution can be given without any ambiguity.

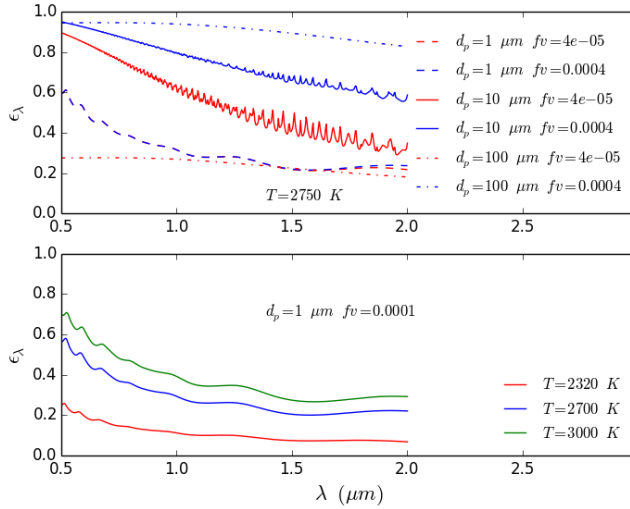


FIG. 12 – Spectral emissivity for different values of temperature, Alumina particle diameter and volume fraction

Unlike Goroshin’s method [11] and Lynch’s model [26], this mathematical inversion method gets rid of any assumption on the particle cloud global emissivity with the wavelength. In our method, the emissivity is physically modeled which leads to a regularization of the mathematical inversion. This thermal emission model represents accurately both the micro alumina particle cloud spectral emissivity tendencies measured by Lynch [26] and the classic optical thickness evolutions with particle size and volume fraction. Applied to synthetic radiances computed with the direct model, the mathematical inversion retrieves both the given temperature and mean particle diameter. It has also been validated by measurements on Al_2O_3 calibrated particle clouds heated by deflagration of gaseous mixtures as explained in the following section.

VI. EXPERIMENTAL CONDITIONS AND RESULTS

Two levels of deflagration pressure have been investigated. The experimental initial conditions have been chosen to produce deflagration pressure ranges of 7.3-8.8 bar (Group A) and 15.5-18.2 bar (Group B). They are given in Table 2, together with the thermal diagnostics used (IR or Vis-nIR) and the final deflagration state (gas pressure and temperature). Calculated particle cloud temperatures and mean diameters from the previous inversion method are given in Table 3. Uncertainties on the final gas deflagration pressure are evaluated at 1.5 % for Group A and at 3.9 % for Group B, based on five experiments for each group, with a probability of 95 % (corresponding to two standard deviations). Maximum uncertainty on gas temperature, established with the uncertainties propagation method described in [29], is evaluated at 1.6%. Uncertainties on particle diameter and temperature are estimated by Monte-Carlo drawings applied on the direct model, thanks to which the maximum values determined are respectively of 23.1 % and 2.3 % with a probability of 95 %. Particle temperature uncertainty is

consequently greater than gas temperature one, due to the propagation of n, k, λ and measured radiances uncertainties.

TABLE 2: Experimented mixtures (initial molar fractions), initial and final deflagration pressures, thermal diagnostics (IR : 4.10–4.30 μm , Vis-nIR : 0.660–1.481 μm) and gas temperatures. The initial temperatures are in the range of 293 K to 300 K.

Group	Shot	x_{N_2}	x_{H_2}	x_{O_2}	x_{CO_2}	x_{CO}	$x_{\text{Al}_2\text{O}_3}$	x_{Al}	P_{initial} (bar)	P_{final} (bar)	Thermal diag.	T_{gas} (K)
A gas	R16	0.199	0.405	0.209	0.187				1.07	7.90	IR	2924
	R17	0.005	0.397	0.201	0.402				1.01	7.10	IR	2629
	R18	0.004	0.221	0.112	0.668				1.81	6.40	IR	1594
	R20	0.207	0.393	0.203	0.198				1.01	7.50	IR	2965
	V1	0.208	0.395	0.198	0.199				1.01	7.70	IR	2952
	V8	0.205	0.397	0.199	0.200				1.02	7.76	IR	2930
	L1	0.203	0.398	0.200	0.199				1.01	7.76	IR	2930
	L3	0.203	0.398	0.200	0.199				1.02	7.34	Vis-nIR	-
B gas	R14	0.110	0.523	0.263	0.105				1.91	16.10	IR	3572
	R19	0.111	0.524	0.260	0.105				1.92	17.50	IR	3500
	V2	0.110	0.522	0.262	0.105				1.93	17.22	IR	3490
	V9	0.107	0.525	0.262	0.106				1.92	16.46	IR	3500
	L2	0.107	0.525	0.263	0.105				1.91	16.46	IR	3500
	L4	0.107	0.525	0.263	0.105				1.92	17.04	Vis-nIR	-
gas + CO	V5	0.434	0.285	0.141	0.106	0.034			1.42	10.2	IR	2744
	V6	0.354	0.343	0.171	0.099	0.034			1.47	11.7	IR	3071
	V7	0.357	0.355	0.174	0.085	0.030			1.74	13.66	IR	3123
A gas + Al ₂ O ₃	R22	0.192	0.370	0.190	0.171		0.078		1.10	7.50	IR	2438
	V3	0.194	0.372	0.186	0.172		0.077		1.19	8.09	IR	2435
	L5	0.186	0.366	0.184	0.183		0.081		1.04	7.47	IR	2435
	L7	0.186	0.366	0.184	0.183		0.081		1.04	7.47	Vis-nIR	-
	R21	0.110	0.495	0.251	0.099		0.046		1.93	15.50	IR	2876
B gas + Al ₂ O ₃	V4	0.111	0.4962	0.2481	0.0992		0.046		2.03	15.89	IR	2865
	L6	0.102	0.502	0.251	0.101		0.044		1.95	16.00	IR	2865
	L8	0.102	0.502	0.251	0.100		0.045		1.95	16.00	Vis-nIR	-
A gas + Al	V10	0.159	0.296	0.148	0.145			0.253	1.38	8.83	IR	2970
	L9	0.178	0.349	0.176	0.175			0.122	1.03	8.830	IR	2970
	L11	0.173	0.339	0.170	0.169			0.149	1.03	8.80	Vis-nIR	-
	L12	0.194	0.382	0.192	0.191			0.041	1.02	8.50	Vis-nIR	-
B gas + Al	V11	0.096	0.441	0.221	0.089			0.153	2.28	18.16	IR	3665
	L10	0.099	0.486	0.243	0.097			0.075	1.92	18.20	IR	3665
	L13	0.105	0.513	0.257	0.103			0.022	1.92	18.00	Vis-nIR	-

Table 3 summarizes the results: mean deflagration gas pressure and temperature, Al₂O₃ particle cloud temperature, mean diameter, emissivity, and related figures. These data are compared with temperatures and gray body emissivity computed following Goroschin’s method [11]. This method leads to non-physical emissivity for the Shot L13. Temperature discrepancies between the two methods are of at least 100 K.

TABLE 3: Inversion results: final deflagration pressure, final gas temperature, final temperature of the particles, smoke mean size and uncertainties, emissivity obtained after inversion, values obtained by Goroshin in [11]

Group	Mixture	Shots	Mean P_{gas} (bar)	Mean T_{gas} (K)	$T_{\text{Al}_2\text{O}_3}$ (K)	Al_2O_3 vol. fraction	d_{part} (μm)	$\varepsilon_{850\text{nm}}$	T_{part} [11] (K)	ε [11]	Fig.
A	gas	L1, L3, R20, V1, V8	7.62 ± 0.11	2944 ± 47	-	-	-	-	-	-	13,14, 16
	gas + Al_2O_3	L5 ,L7, R22,V3	7.47 ± 0.11	2436 ± 39	$< T_{\text{fus}}$	$0.97 \cdot 10^{-4}$	-	-	2380	0.1	no fig.
	gas + Al	L11	8.80 ± 0.13	2970 ± 47	2786 ± 64	$1.83 \cdot 10^{-4}$	2.6 ± 0.6	0.6	2905	0.5	16
		L12	8.50 ± 0.12	-	2630 ± 61	$0.50 \cdot 10^{-4}$	2.1 ± 0.5	0.5	2767	0.4	
B	gas	L2, L4, R14, V9,R19	16.61 ± 0.64	3518 ± 56	-	-	-	-	-	-	14,15
	gas + Al_2O_3	L6, L8, R21,V4	15.85 ± 0.62	2869 ± 46	2548 ± 59	$0.97 \cdot 10^{-4}$	43 ± 11	0.7	2709	0.5	15
	gas + Al	L13	18.00 ± 0.70	3665 ± 59	2727 ± 63	$1.83 \cdot 10^{-4}$	18.4 ± 4.3	0.9	2624	1.2	17.

VII.DISCUSSION

A. Gas

A typical evolution of the radiance intensity measured in the IR range (4.1-4.3 μm) is presented as a function of time on the right side of Fig. 13. The lower curve ($t=1$ ms) corresponds to the beginning of the flame propagation inside the gaseous mixture, just after its ignition. The highest curve ($t=15$ ms) has been recorded when the flame has reached the sapphire window corresponding to the maximum of the pressure signal as illustrated on the left side of Fig. 13. This pressure evolution is classically observed in such a confined configuration ([12] [16] [20]). These records exhibit the maximum of the CO_2 emission line and the absorption of this radiation by the cold CO_2 in the fresh gases in front of the flame. The intensity of the maximum radiance increases. Simultaneously, the absorption of cold CO_2 in the fresh gas decreases when the front flame moves towards the sapphire window, because of the reduction of the fresh gaseous mixture thickness. However, to observe this decrease, thickness must be small enough. The last curve (obtained here at 15 ms) corresponds to the radiation emitted by heated CO_2 in the burned gases. This last curve is exploited to determine gas temperature by considering that the head of the 4.26 μm CO_2 emission band behaves like a blackbody. The results obtained for Groups A and B are given on Fig.14. This figure highlights the CO_2 head band shift due to the elevation of pressure and temperature. The HITRAN computations overestimate this shift as suggested by Fig. 6.

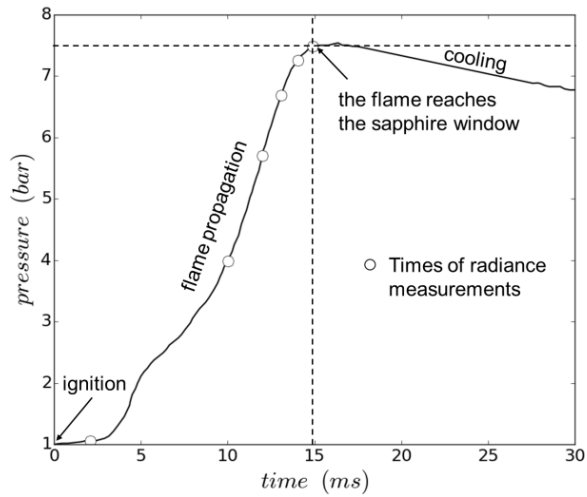


FIG. 13a

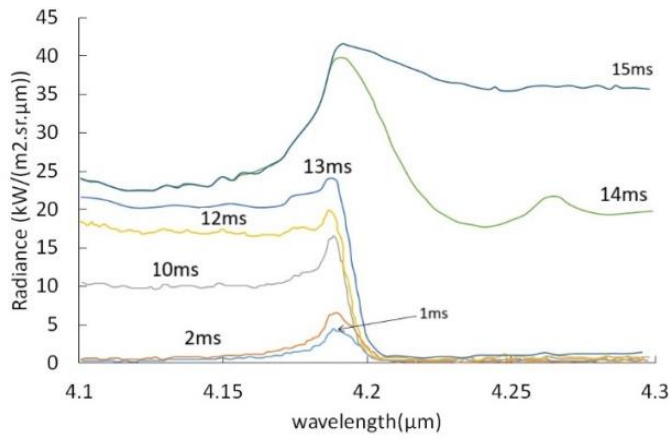


FIG. 13b

FIG.13: Measured pressure (13a) and radiances in experiment L1 in the IR range at several times (13b)

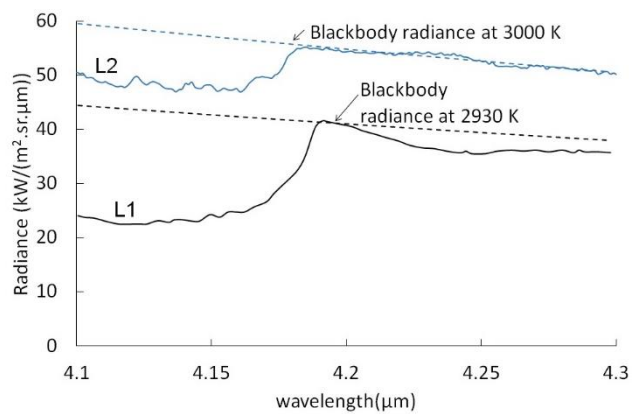


FIG.14: Measured radiances in experiments L1 and L2 in the IR range when the deflagration reaches the sapphire window.

B. Validation of the inversion method on the deflagration of gas – Al_2O_3 particle mixtures

For Group A, the inversion method applied in the VIS-nIR wavelength range gives a temperature lower than Al_2O_3 melting temperature (2320 K). By considering the optical index of solid alumina, the transmission

coefficient is supposed to be greater than 0.9. This value suggests then that, in the conditions of Group A, the measured flux comes both from plug and particle emission. The method is consequently no longer valuable.

For Group B, the radiances measured with and without particles are given on Fig. 15. Particles are at 2548 K and have melted. The particle temperature is significantly lower (at least 317 K) than the gas temperature. The gas and particles are not in thermal equilibrium as physically expected. The diameter of the injected particles is retrieved by the inversion method.

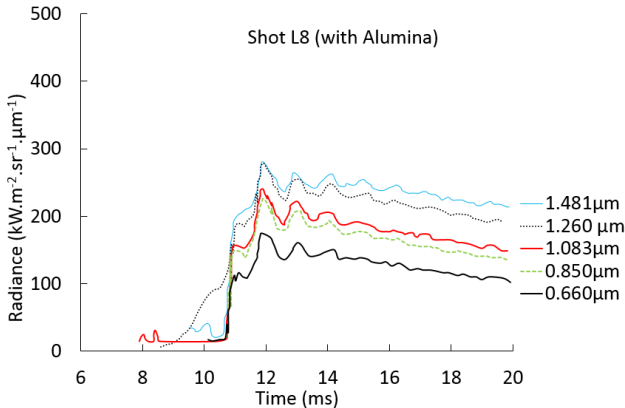


FIG. 15a

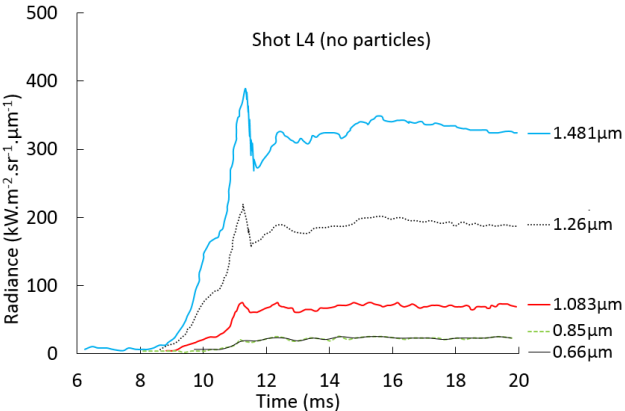


FIG. 15b

FIG. 15: Results for shots L4 and L8

C. Application to the deflagration of gas – Al particles mixtures

Group A evolutions of the measured radiance intensity in the VIS-nIR range are presented as a function of time for a deflagration with and without 4 g of aluminum (L11 and L3, Fig.16). For L3, no significant radiance has been recorded at the wavelengths of 0.660 and 0.850 μm. The radiances registered at 1.481 and 1.260 μm, probably coming from the hot spark igniter, are consequent compared to particle radiation. Hence, 1.481 and 1.260 μm signals of Shot L11 have not been used in the radiative heat transfer equation inversion. At the

wavelength $1.083\ \mu\text{m}$, a transmission coefficient of 0.48 and a temperature of 2785 K have been obtained thanks to the inversion method. This confirms a negligible parasite flux at this wavelength. Although the alumina smoke dimensions deduced from the experiments are micronic (Table 3), they are in a thermal non-equilibrium with regards to the surrounding gas since their temperatures are $184\pm 10\ \text{K}$ lower than that of gas deduced from the IR signal of experiment L11 as described in section VII-A. As expected, radiance intensity in the Vis range increases with the amount of aluminum.

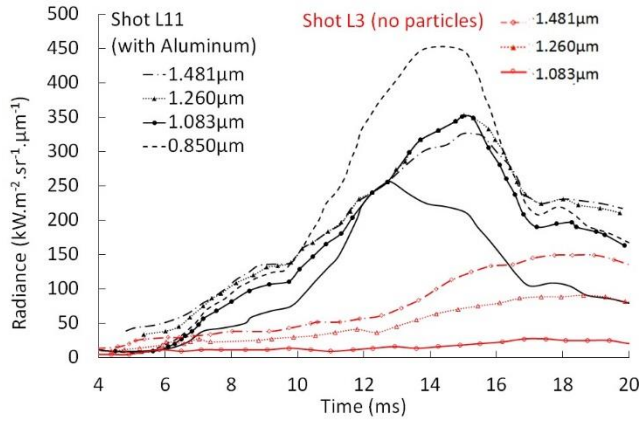


FIG.16: Measured radiances in experiments L3 and L11

Group B evolutions of the radiance intensity measured in the VIS-nIR range are presented as a function of time for a deflagration with and without 4 g of aluminum (L13 and L4, Fig.17). A signal was recorded for all the pyrometer channels. As previously, the signals at $1.481\ \mu\text{m}$ and $1.260\ \mu\text{m}$ are not retained for the inversion of the radiative equation. The particle diameter is still micronic. The gas temperature is greater than that of Group A whereas Al_2O_3 droplet temperature is similar. Thermal equilibrium is here again not achieved.

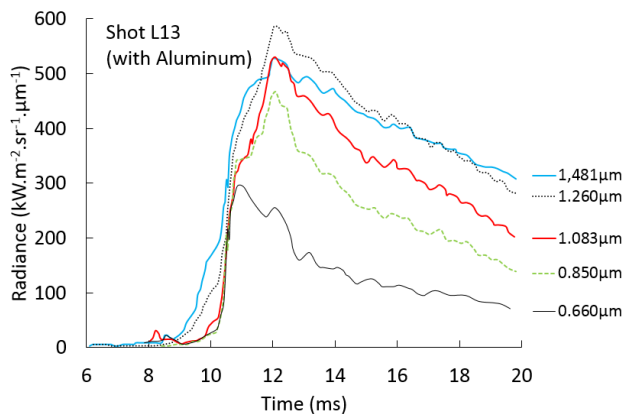


FIG. 17a

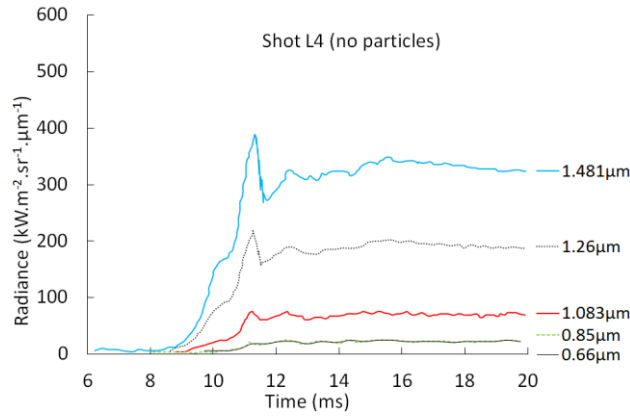


FIG. 17b

FIG.17: Measured radiances as a function of time for Shots L13 and L4

D. Comparison with thermochemical computations

Deflagration products, temperatures and pressures are calculated with the thermochemical code SIAME by considering an adiabatic constant volume explosion under the assumption that pressure and temperature are in equilibrium between particles and gas. The real gas BKW equation of state for the gaseous mixture and the Cowan equation of state for condensed species (C, Al, Al_2O_3) [29] are used with the BKWC database published in [30]. In the case of aluminum additives, the computations are performed considering unburned (inert) or totally burned (reacted) particles. The computed temperatures and pressures are compared to the experimental data on Fig.18 and Fig.19.

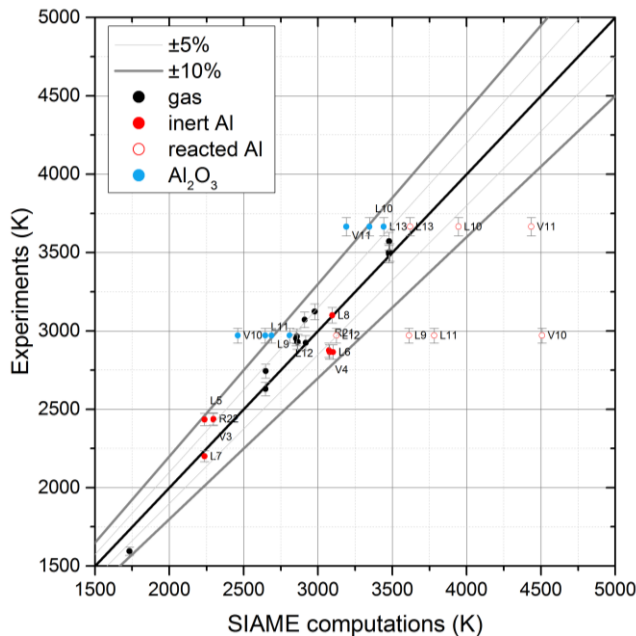


FIG.18: Comparisons between computed and experimental gas temperatures.

For shots without particles, the maximum deviations between experiments and computations are 11 % for pressures and 8 % for temperatures. They are below the classical error-bars of thermochemical computations.

For shots with aluminum particles, the maximum deviations on pressure between experiments and computations reaches +90 %, when assuming totally burned particles. However, when considering non-reactive particles, it reaches -13 %. The experimental pressure is systematically close to the computed one when unburned aluminum particles are considered. For temperature, the maximum deviation reaches +51 % when assuming totally burned particles and -17 % when unreacted particles are considered. Experimental temperature is always between the totally burned and unburned aluminum computed values for initial molar fractions of 0.149 and 0.075. Initial particle content strongly influences gas and alumina cloud temperatures. The thermochemical code is unable to predict these effects.

For alumina, computation systematically overestimates pressure and temperature with maximal deviations of respectively 14 % and 8 %.

The discussion on experimental data and the good accuracy of the thermochemical computations for gas mixtures have led to the conclusion that non-equilibrium between particles and gas, which is not-taken into account in SIAME, does not strongly influence the deflagration pressure. Lack of sensitivity of the emission model to the volume fraction of alumina particles makes difficult to conclude about the aluminum total combustion or lack of it in the deflagration wave.

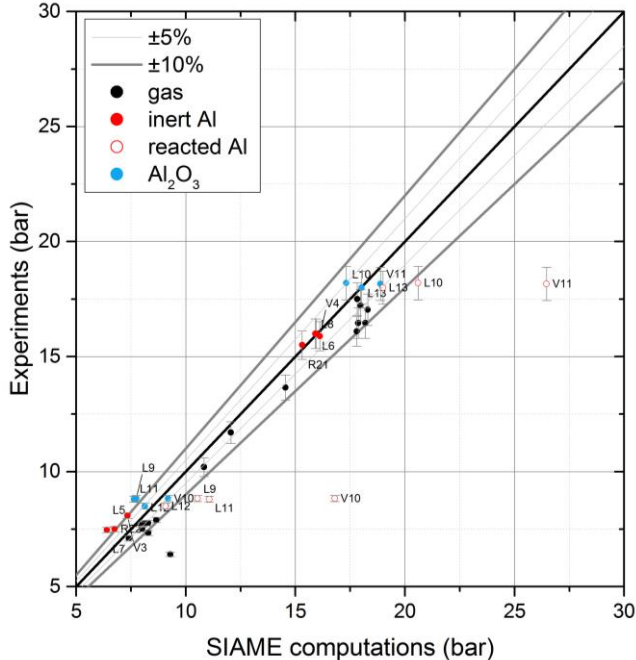


FIG.19: Comparisons between computed and experimental pressures.

VIII. SUMMARY AND CONCLUSION

The emission of gas and Al_2O_3 smoke in $\text{H}_2\text{-O}_2\text{-}\{\text{N}_2\text{-CO}_2\}$ -Al deflagration has been measured in a closed combustion chamber up to 17 bar and 3700 K. Measurements have been performed in the VIS-nIR range of wavelengths for smoke and in the IR spectral range 4.10-4.30 μm for the CO_2 emission lines. Gas temperature has been deduced from the radiation intensity measured at the head of the 4.26 μm CO_2 emission band. This radiation intensity has been considered as the one emitted by a blackbody and it has appeared to be very sensitive to gas temperature.

From the Vis-nIR experimental results, an inversion method has been developed to evaluate Al_2O_3 particle cloud temperature and mean diameter, formed by aluminum combustion, by considering a two-stream approximation of the radiative heat transfer equation and the Mie scattering model. This method has been validated thanks to a calibrated Al_2O_3 suspension heated by gaseous deflagrations: particle mean size is retrieved, gas cooling and thermal non equilibrium between gas and particles have been observed, as physically expected.

The method was applied to Al_2O_3 smoke generated by $\text{H}_2\text{-O}_2\text{-}\{\text{N}_2\text{-CO}_2\}$ -Al deflagrations. Experimental results have been compared to thermochemical calculations obtained with the SIAME code developed by CEA:

- for gas mixtures, calculated and experimental data are in good agreement and within 11% error for pressure and 8% for temperature.
- for particle and gas mixtures, experimental temperatures have been found between those calculated considering either inert or totally reacted aluminum, whereas calculated pressures obtained when considering inert aluminum have been observed to be closer to the experimental ones.

Initial aluminum concentration strongly influences cloud emissivity and consequently, gas and Al_2O_3 particle temperatures. For the experimented volume fractions of Al particles, Al_2O_3 smoke clouds are optically thin. This Al volume fractions range leads to an Al_2O_3 smoke volume fraction of about 10^{-4} , which is representative of explosive fireball expansions. The originality of the proposed inversion method applied to radiance measurements is that thermal non-equilibrium between gas and particles is assumed. Yet, this thermal non-equilibrium has had to be left aside in the thermochemical SIAME calculations. More effort is still needed to characterize the effects of aluminum initial concentrations and particle – gas non-equilibrium in the thermochemical computations.

ACKNOWLEDGMENTS

Support of this work from the French Ministry of Defense, DGA, is gratefully acknowledged.

The authors are grateful to Vladimir M. Belski from the Russian Federal Nuclear Center-VNIIEF, Institute of Physics of Explosion, Sarov, Nizhni, Novgorod, Russia, for their help to characterize the -200 mesh Aldrich aluminum powder. They are also grateful to the anonymous referees and to the English advisors for their valuable help in improving the quality of the manuscript.

REFERENCES

1. A.L. Kuhl, "Mixing in explosion, Lawrence Livermore National Laboratory", Livermore, Report, UCRL-JC-115690, (1993).
2. L. Munier, PhD Thesis, Univ. Provence, Aix Marseille I, France, (2011).
3. L.E. Fried, W.M. Howard, P.C. Souers, Cheetah 2.0 user's manual, Lawrence Livermore National Laboratory, Livermore, CA, Report, UCRL-MA-117541, Rev. 5, (1998).
4. L.S. Rothman, I.E. Gordon, A. Barbe, D. Chris Benner, P.F. Bernath, M. Birk, V. Boudon, L.R. Brown, A. Campargue, J.-P. Champion, K. Chance, L.H. Coudert, V. Dana, V.M. Devi, S. Fally, J.-M. Flaud, R.R. Gamache, A. Goldman, D. Jacquemart, I. Kleiner, et al, J. Quant. Spectrosc. Rad. Transfer, **110** (9-10) 533-572, (2009)
5. L.S. Rothman et al, J. Quant. Spectrosc. Rad. Transfer, **130** (9-10) 4-50, (2013)
6. L.S. Rothman, I.E. Gordon, R.J. Barber, H. Dothe, R.R. Gamache, A. Goldman, V. Perevalov, S.A. Tashkun, and J. Tennyson, J. Quant. Spectrosc. Rad. Transfer **111** 2139-2150, (2010)
7. S.A. Tashkun, V.I. Perevalov, J. Quant. Spectrosc. Rad. Transfer **112** (9) 1403-1410, (2011)
8. M.F. Modest - *Radiative Heat Transfer*, Mc Graw-Hill, 1993.
9. C. Badiola, R.J. Gill, E.L. Dreizin, Combust. Flame **158** 2064-2070, (2011).
10. X. Zhu, M. Schoenitz, E.L. Dreizin, J. Phys. Chem. C **113**, 6768-6773, (2009).
11. S. Goroshin, J. Mamen, A. Higgins, T. Bazyn, N. Glumac, H. Krier, Proc. Combust. Inst. **31**, 2011-2019, (2007).
12. P. Escot Bocanegra, Ph.D.thesis, Univ. Orléans, France, (2007)
13. D.L. Parry, M.Q. Brewster, J. Thermophysics, **5** (2) 142-149, (1991).
14. S. Goroshin, D.L. Frost, J. Levine, A. Yoshinaka, F. Zhang, Prop., Explos., Pyrotech. **31** (3) 169-181, (2006).
15. K.L. Cashdollar, I.A. Zlochower, J. Loss Prev. Process Ind., **20** 337-348, (2007).

16. P. Chelin, C. Camy-Peyret, V. Pina, P. Alkhoury and D. Davidenko, *Combust. Flame*, **140** 319-331 (2005)
17. A. Lefrançois, G. Baudin, C. Le Gallic, P. Boyce, J.P. Coudoing, Proceedings of the 12th International Conference Symposium on detonation, San Diego, California, (2002).
18. C.L. Tien, B.L. Drolen, *Annual review of numerical fluid mechanics and heat transfer* **1** 1-32 (1987)
19. D. Davidenko, , PhD Thesis, Univ. Orleans, France (2005)
20. P.R. Santhanam, E.L. Dreizin, “Characteristics of metal combustion obtained from constant volume explosion experiments”, 48th AIAA Aerospace Sciences Meeting, Orlando, Florida, paper 2010-0178, (2010).
21. D. Ramel, PhD Thesis, Univ. Paris Nanterre, France, (2008).
22. M.W. Beckstead, Brigham Young Univ. Provo, Utah, USA, (2004).
23. M.W. Beckstead, Liang Y., and K.V. Pudduppakkam, *Combust., Explos. Shock Waves*, **41**, n°6, 622-638, (2005).
24. R. H. French, H. Müllejans, and D. J. Jones, *J. Am. Ceram. Soc.*, **81**(10), 2549 (1998).
25. V. K. Bitjukov, V. A. Petrov, *Appl. Phys. Research*, **5** (1) 51-71, (2013)
26. P. Lynch, H. Krier and N. Glumac, *J. Thermophysics*, **24** (2) 301-308, (2010)
27. C.F. Bohren, D.R. Huffman, *Absorption and Scattering of Light by Small Particles*, Wiley, New York, (1983)
28. Meador W.E. and Weaver W.R., *J. atmos. Sci.* **37**, 630-643 (1980)
29. BIPM, IEC, IFCC, ISO, IUPAC, IUPAP and OIML guide to the expression of uncertainty measurement 2nd edition, ISBN 92-67-10188-1995 (French normative document NF ENV 13005), (1995).
30. Fried E.L. and Souers P.C., *Propellants, Explosives, Pyrotechnics*, **21** (4), 215-223 (1996).